

## Searching for compact objects in binaries with *Gaia* DR3

JIN-BO FU,<sup>1</sup> WEI-MIN GU,<sup>1</sup> ZHI-XIANG ZHANG,<sup>1</sup> TUAN YI,<sup>1</sup> SEN-YU QI,<sup>1</sup> LING-LIN ZHENG,<sup>1</sup> AND JIFENG LIU<sup>2,3</sup>

<sup>1</sup>*Department of Astronomy, Xiamen University, Xiamen, Fujian 361005, China*

<sup>2</sup>*National Astronomical Observatories, Chinese Academy of Sciences, Beijing 100101, China*

<sup>3</sup>*College of Astronomy and Space Science, University of Chinese Academy of Sciences, Beijing 100049, China*

### ABSTRACT

We search for compact objects in binaries based on *Gaia* DR3. A sample of ten targets is derived under the conditions: radial velocity variable, low temperature ( $T_{\text{eff}} < 6000$  K), high mass function ( $f(M_2) > 1M_{\odot}$ ), and ellipsoidal-like light curves. Two targets have LAMOST spectroscopic observations, one of which is a double-lined spectroscopic binary. The observational data of seven targets are not self-consistent, since their photometric periods are even shorter than the theoretical minimum orbital periods calculated by the stellar parameters from *Gaia* DR3. After excluding these seven inconsistent targets and another target contaminated by a near-bright star, the remaining two targets may contain compact objects worth follow-up observations. This work may serve as an example to demonstrate the feasibility of searching for compact objects in the massive *Gaia* data.

**Keywords:** Close binary stars (254), Compact binary stars (283), Light curves (918), Radial velocity (1332), Spectroscopic binary stars (1557)

### 1. INTRODUCTION

Dynamical searching and identification of binary systems by spectroscopic surveys has made progress in recent years, especially for quiescent (e.g., without accretion) binary systems that contain compact objects (black holes, neutron stars, and white dwarfs, e.g., Casares et al. 2014; Thompson et al. 2019; Liu et al. 2019; Rivinius et al. 2020; Jayasinghe et al. 2021; Hernandez et al. 2021; Saracino et al. 2022; Lam et al. 2022; Shenar et al. 2022; Mazeh et al. 2022). Several such compact object candidates have been proposed from spectroscopic surveys (e.g. Rebassa-Mansergas et al. 2016; Cojocaru et al. 2017; Rebassa-Mansergas et al. 2017; Ren et al. 2018; Gu et al. 2019; Zheng et al. 2019; Mu et al. 2022; Zhang et al. 2022). Besides, X-ray surveys are vital for searching for compact objects within accreting binaries (Remillard & McClintock 2006; McClintock & Remillard 2006), and gravitational wave observations are successful in detecting compact objects from mergers (Abbott et al. 2016). These three approaches provide plentiful candidates that can

be used to study the mass distributions and characterize the populations of compact objects.

The samples of compact object candidates can be potentially enlarged greatly (e.g. Gomel et al. 2022) thanks to the *Gaia* Data Release 3 (*Gaia* DR3; Recio-Blanco et al. 2022), which provides astrometry, photometry, and spectroscopy for stars with an unprecedented scale. For instance, astrometry analyses are expected to uncover about 190 compact binaries from *Gaia* DR3 (Janssens et al. 2022). Recently, a promising candidate *Gaia* BH1 has been proposed utilizing the astrometric solution from *Gaia* DR3 (El-Badry et al. 2022). Furthermore, the radial velocity variations ( $\Delta V_r$ ) of 6,981,248 targets taken with the RVS instrument are firstly among the available data products (Recio-Blanco et al. 2022), which can facilitate the searching for compact objects from a dynamical perspective. The wavelength coverage of the  $V_r$  instrument is 846-870 nm, with a typical spectral resolution of about 11,500 (De Angeli et al. 2022; Montegriffo et al. 2022). *Gaia* DR3 also provides a variety of labels for each object (Holl et al. 2022), like single-lined spectroscopic binary (SB1) and double-lined spectroscopic binary (SB2) classifications, temperatures and radii (Hambly et al. 2022), which contribute to better characterizing the parameters of the stellar systems.

A proper method can facilitate the filtering of interesting targets from *Gaia*'s massive data products. The minimum orbital period ( $P_{\text{orb}}^{\text{min}}$ ) of a binary system can be calculated

Corresponding author: Wei-Min Gu, Zhi-Xiang Zhang, Tuan Yi

guwm@xmu.edu.cn  
zhangzx@xmu.edu.cn  
yit@xmu.edu.cn

using the mass ( $M_1$ ) and radius ( $R_1$ ) of its visible component (Gu et al. 2019; Zheng et al. 2019), and the minimum mass function  $f(M_2)$  of its invisible component can be calculated using the  $\Delta V_r$  of its hosting system. Therefore, by requiring a lower limit on the mass function, we can select potential hidden compact objects in binary systems that are not visible optically.

The above approach relies only on the data provided by *Gaia*. Nevertheless, more data would increase the credibility of the selected samples. For instance, multi-band spectral energy distributions (SEDs) and light curves contribute to judging whether a binary system is composed of two visible stars (El-Badry & Rix 2022). The spectroscopic surveys (e.g. the Large Sky Area Multi-Object Fiber Spectroscopic Telescope; LAMOST; see Cui et al. 2012; Zhao et al. 2012) can help to determine whether the target is a binary system (Merle et al. 2017; Li et al. 2021), and whether the radial velocity variation is credible.

Based on the above methodology, we first select a raw sample with high mass function from *Gaia* DR3, then utilize the high-precision light curves from the Transiting Exoplanet Survey Satellite (*TESS*, Ricker et al. 2015) to find ellipsoidal variables (Morris 1985; Morris & Naftilan 1993; Gomel et al. 2021; Rowan et al. 2021), and fitting the broad-band SEDs to validate the radii and temperatures provided by *Gaia*. Further validation is done by using spectroscopy from LAMOST to exclude binary stars and derive the candidates.

The rest of this paper is organized as follows. Observations and data reduction are described in Section 2. The selected targets are analyzed in detail in Section 3, followed by our main conclusions in Section 4.

## 2. DATA SELECTION AND PROCESSING

### 2.1. *Gaia*

We begin by filtering the *Gaia* DR3 database<sup>1</sup> with the following criteria to identify the velocity variable stars and obtain their radial velocity variations  $\Delta V_r$  (`rv_amplitude_robust`):

- `rv_nb_transits`  $\geq 10$ ,
- `rv_template_teff`  $\leq 8000$  K,
- `rv_chisq_pvalue`  $\leq 0.01$ ,
- `rv_renormalised_gof`  $> 4$ , and
- `teff_gspphot`  $< 6000$  K,

where the first four criteria are suggested by Katz et al. (2022), and the last one is to ensure the exclusion of hot stars

(defined as  $T_{\text{eff}} > 6000$  K), which may suffer more considerable RV uncertainties (Blomme et al. 2022). The above RV cuts reduced the number of candidates to 328,621. We additionally applied astrometric and photometric quality cuts to exclude targets with large distance measurement errors and potentially inaccurate photometry, which further shrinks the number of targets to 317,278:

- `parallax_over_error`  $> 5$ ,
- `phot_bp_rp_excess_factor`  $< 3$ .

A more detailed description of these properties can be found in Hambly et al. (2022). We require that the masses and radii provided by *Gaia* are not null, and use them to obtain the theoretical minimum orbital period of the remaining 284,607 binary systems (Zheng et al. 2019):

$$P_{\text{orb}}^{\text{min}} = 2\pi \left[ \frac{(R_1/0.462)^3}{GM_1} \right]^{1/2}, \quad (1)$$

where  $M_1$ ,  $R_1$  is the mass and radius of the optically visible star. The mass function of the invisible star can then be expressed as (Remillard & McClintock 2006):

$$f(M_2) = \frac{M_2^3 \sin^3(i)}{(M_1 + M_2)^2} = \frac{K_1^3 P_{\text{orb}}}{2\pi G}, \quad (2)$$

where  $K_1 \geq \Delta V_r/2$  is the semi-amplitude of the radial velocity, and  $P_{\text{orb}} \geq P_{\text{orb}}^{\text{min}}$  is the orbital period of the target. Finally, to select those potential compact objects, we require

- $f(M_2) > 1 M_{\odot}$ .

The above steps yield 65 targets from the *Gaia* DR3 database.

Figure 1 shows the theoretical minimum orbital period and semi-amplitude of velocity variations of the 65 selected targets. Two targets (Gaia ID: 5200508962219751424 and 2066328011855804544) have theoretical minimum orbital periods  $P_{\text{orb}}^{\text{min}} > 100$  days. The long periods are due to their large radii of  $178 R_{\odot}$  and  $125 R_{\odot}$  measured by *Gaia* (see supplement Table 2). Their radii are much larger than other selected targets ( $\sim 8.5 R_{\odot}$  on average), leading to longer theoretical minimum orbital periods (Equation 1). These two objects are excluded from our final samples due to their *TESS* light curves (see Section 2.2).

### 2.2. *TESS* photometry

Using `lightkurve`<sup>2</sup>, we retrieve the 65 targets listed in Table 2 and download available photometric data for 55 of them from *TESS*. We obtain the photometric period for each target using the Lomb-Scargle periodogram (Press & Rybicki 1989), which is then used to phase-fold the light

<sup>1</sup> <https://gea.esac.esa.int/archive/>

<sup>2</sup> <https://docs.lightkurve.org>

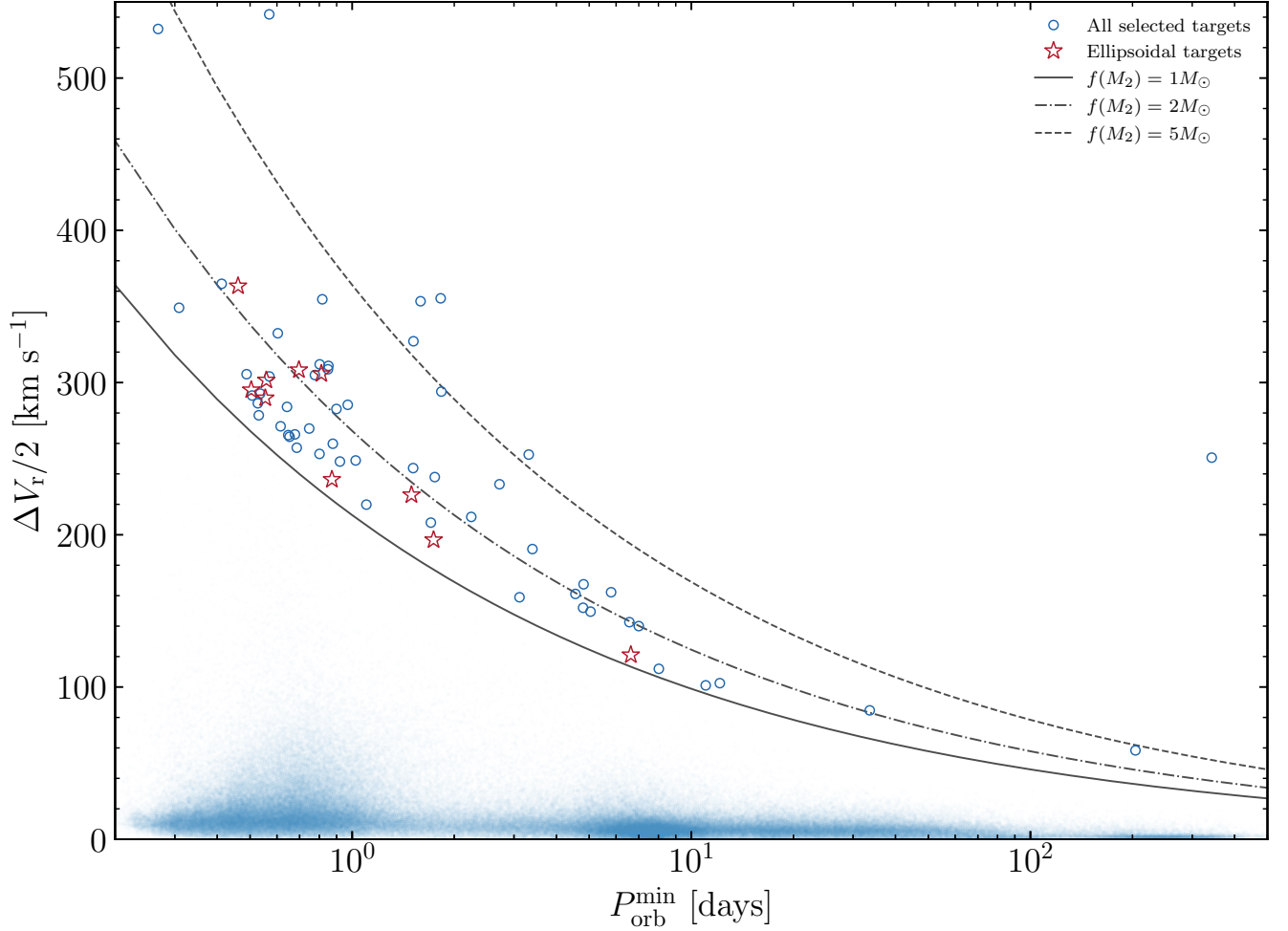


**Figure 1.** A sample of 65 targets selected from *Gaia* DR3. The ten red pentagrams indicate the targets presented in Table 1. The solid, dot-dashed, and dashed lines each corresponds to a fixed value of the mass function. To demonstrate the distribution of the mass functions, we show all the 278,536 targets that satisfy the criteria described in Section 2 for comparison, represented by blue points (blurred for reducing the size of the figure).

curve. For targets with multiple *TESS* sectors observed, the sector with the longest observation time span is used. We reject targets with a folded photometric period  $P_{\text{orb}}^{\text{lc}} > 15$  days, since each *TESS* sector has at most 27 days of time coverage (Ricker et al. 2015). We visually inspect and manually classify the phase-folded light curves into: (1) ellipsoidal variables (tidally distorted stars which may contain a hidden compact object), (2) eclipsing binaries (binary stars show occultations periodically), and (3) irregular variables (such as eruptive stars, spotted rotational variables, variability of unknown origin, and variability of non-variables due to systematic effects of *TESS*). Figure 2 shows three cases for each variable class as examples. We found and discarded 29 eclipsing binaries with 16 irregular variables. The remaining ten sources have ellipsoidal-like light curves (Figure 3) and are chosen as the final sample. The photometric periods of these ten targets, and their mass functions calculated from the photometric periods, are listed in Table 1. Note that the

lack of ellipsoidal variability cannot rule out potential massive unseen companions since the ellipsoidal modulation is sensitive to the separation of the two stars. For instance, long period (e.g.  $\gtrsim 10$  days) detached systems may not exhibit ellipsoidal variabilities where a main sequence companion could be subject to negligible tidal distortion from a compact companion. In this paper, we focus on ellipsoidal variables for simplicity.

### 2.3. SED fitting

We measure the surface temperatures and radii of the visible stars of our selected objects by SED fitting. We use the SED fitting to derive robust stellar parameters and therefore to validate that of provided by *Gaia* DR3. Furthermore, we check the goodness-of-fit to evaluate whether a single-star SED model can fit well the data, and thus to verify the possible contaminations from binary systems that contain two stellar components. However, it should be noted that a good

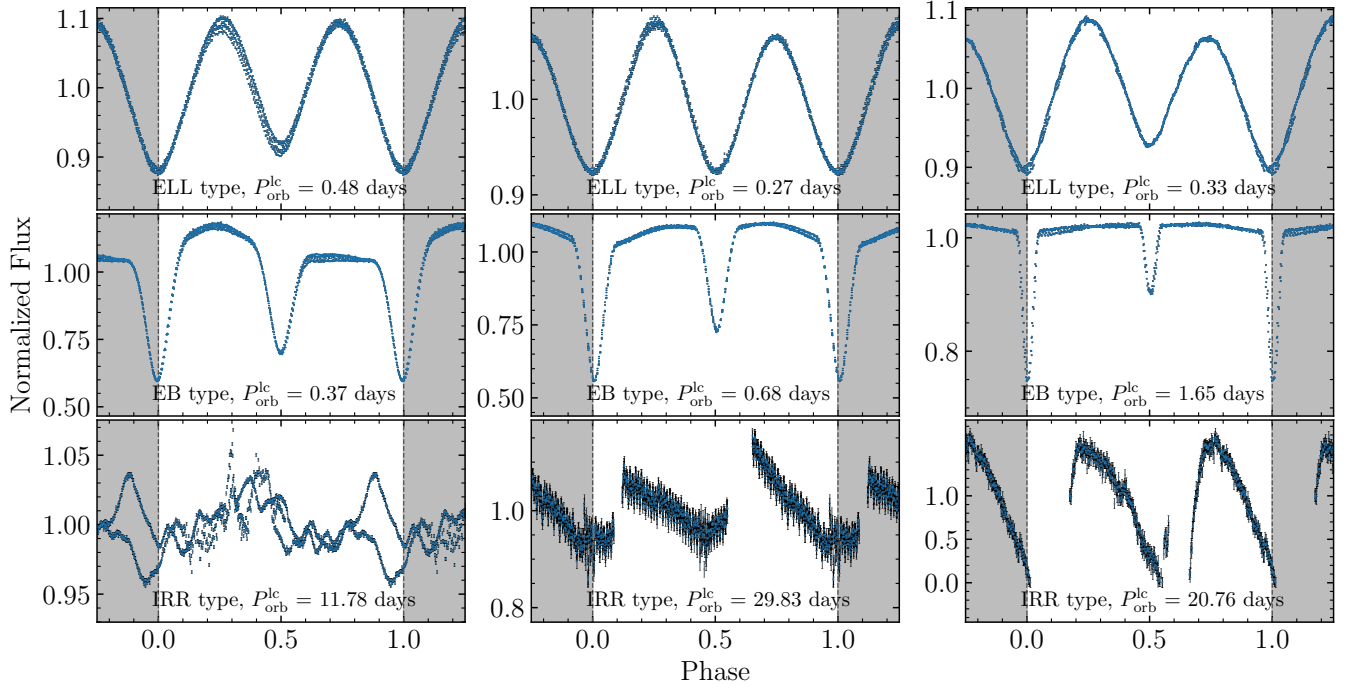


**Figure 2.** Representative *TESS* light curve samples for ellipsoidal variables (ELLs, upper panels), eclipsing binaries (EBs, middle panels), and irregular variables (IRRs, bottom panels). The three ellipsoidal examples correspond to J1631, J1227, and J0056 listed in Table 1, from left to right. The three eclipsing binary samples are *Gaia* 714884906850837120, 2922949687038297088, and 4853820950132560896. The three irregular variables are *Gaia* 2066328011855804544, 2054348862739979648, and 346272671566816512. The properties of eclipsing binaries and irregular variables can be found in Table 2.

SED fitting by a single stellar component does not mean that the SED only has one component. For example, a binary system composed of two stars with similar temperatures can also be well-fitted with a single component.

The fitting is carried out with the help of the *astroARIADNE*<sup>3</sup>, which can automatically download the broadband SED of a given target from UV to IR band and fit it using a set of alternative atmospheric models. The effective temperature ( $T_{\text{eff}}$ ), radius ( $R_1$ ), distance, log surface gravity ( $\log g$ ), metallicity ( $[\text{Fe}/\text{H}]$ ), and line-of-sight extinction ( $A_V$ ) are six fitted parameters. Where the distance and the  $R_1$  are degenerate parameters, we use the distance measured by *Gaia* DR3 as prior to eliminate the degeneracy. The G-band extinctions from *Gaia* are used as a mean of Gaussian prior for each target, since some of them are located near the Milky Way disk and are suffering from high extinctions, thus a uniform prior is not suitable.

The temperatures and radii obtained by the SED fitting are basically consistent with the *Gaia* DR3 results. The SED fitting of temperature and radius for all targets are in agreement with *Gaia*'s results within a  $1.7\sigma$  confidence interval. The median difference for temperature is 115 K and for radius is  $0.1 R_\odot$ . J0709 has the largest measurement difference with

*Gaia*'s result, with a temperature difference of 438 K and a radius difference of  $0.43 R_\odot$ . In the SED fitting of all the selected objects, the models are well-matched with the observed SEDs, and no obvious IR excess is found.

#### 2.4. LAMOST spectroscopy

The LAMOST survey provides both medium-resolution spectra (MRS) and low-resolution spectra (LRS). Typically, two to four consecutive exposures (10-20 minutes per exposure) are taken for each observation. Both single and combined spectra are available. We found two of ten objects have LAMOST observations. One of the objects, J1631<sup>4</sup>, was observed by LAMOST MRS on 2018 May 31 with four consecutive exposures. The other object, J1227, was observed by LAMOST LRS on 2015 Feb 08 with two exposures.

We use the cross-correlation function (CCF) to measure the radial velocities of the LAMOST spectra. The templates are interpolated using *The Payne*<sup>5</sup>, a spectral interpolation tool based on a neural-net algorithm. We use the BOSZ grid (Bohlin et al. 2017) to train the interpolated model. The ef-

<sup>3</sup> <https://github.com/jvines/astroARIADNE>

<sup>4</sup> *Gaia* Source ID: 1410477980245374848. Thereafter, we will use short names to distinguish each target. The *Gaia* source ID of each target and the corresponding short name are listed in Table 1.

<sup>5</sup> <https://github.com/pacargile/ThePayne>

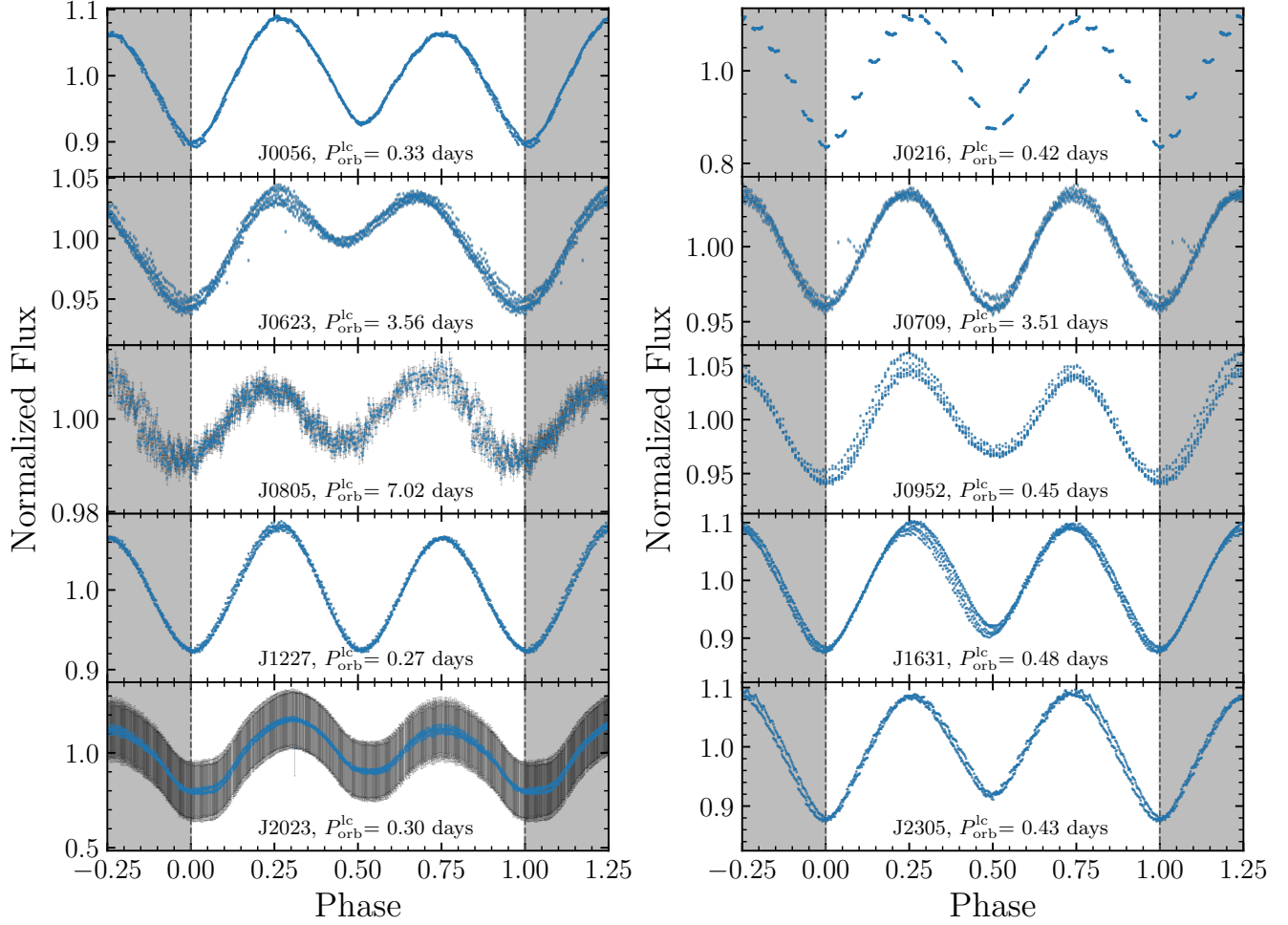


**Figure 3.** The phase-folded *TESS* light curves of the ten targets in Table 1. The primary minimum of each light curve has been shifted to phase 0. Light curves beyond phase 0 - 1 (shaded with gray background) are repeated for clarity.

fective temperatures provided by *Gaia* DR3 are used as prior to choose the model template. The template spectra have been broadened to match the spectral resolution ( $R=7500$ ) of the observed spectra before the training. We find the best stellar parameters by minimizing the  $\chi^2$  of the templates and the observed spectra.

The best fitting stellar parameters of J1631 is  $T_{\text{eff}} = 5700$  K,  $[\text{Fe}/\text{H}] = -1.5$ . The corresponding template is used to measure the RVs of the LAMOST spectra. We find that the template could not match the observed spectra well, and the CCF structures show double peak structures, which indicates that the system could be a SB2 (Figure 4). For the four LAMOST MRS spectra (each exposure time is 20 minutes), we find that the strongest peak on the CCFs fell to near zero and did not move significantly. The second peak has an RV of about  $-250$  km s $^{-1}$ .

To evaluate whether J1631 is a truly SB2, we decompose the spectra of J1631 to obtain the temperatures and RVs of the system more precisely. We use a method similar to El-

Badry et al. (2018) to construct a spectral model for binary systems. The model contains two radiative components, and the two spectra can be adjusted by their corresponding RVs and the flux ratio of the two components. We use Markov chain Monte Carlo (MCMC) method to fit the parameters of the binary spectral model. We assume that the stars of the binary have the same origin and elemental abundance. Therefore, only one set of elemental components needs to be retained in the model. For simplicity, we do not introduce the stellar evolution model in the fitting to constrain the stellar parameters. Finally, our model includes ten free parameters, including  $T_{\text{eff},1}$ ,  $T_{\text{eff},2}$ ,  $\log g_1$ ,  $\log g_2$ ,  $[\text{M}/\text{H}]$ ,  $[\text{C}/\text{M}]$ ,  $[\alpha/\text{M}]$ ,  $V_{r,1}$ ,  $V_{r,2}$ , and the flux ratio of the two spectral components.

Figure 5 shows the best fitting result of the combined spectrum, which gives the temperatures of the two components of  $5931 \pm 23$  K and  $5870 \pm 30$  K. The metal abundance is  $[\text{M}/\text{H}] = -0.26$ . We fixed the stellar parameters to the best fitting results of the combined spectrum and then measured the RVs of each single spectrum. The RVs for the higher tem-



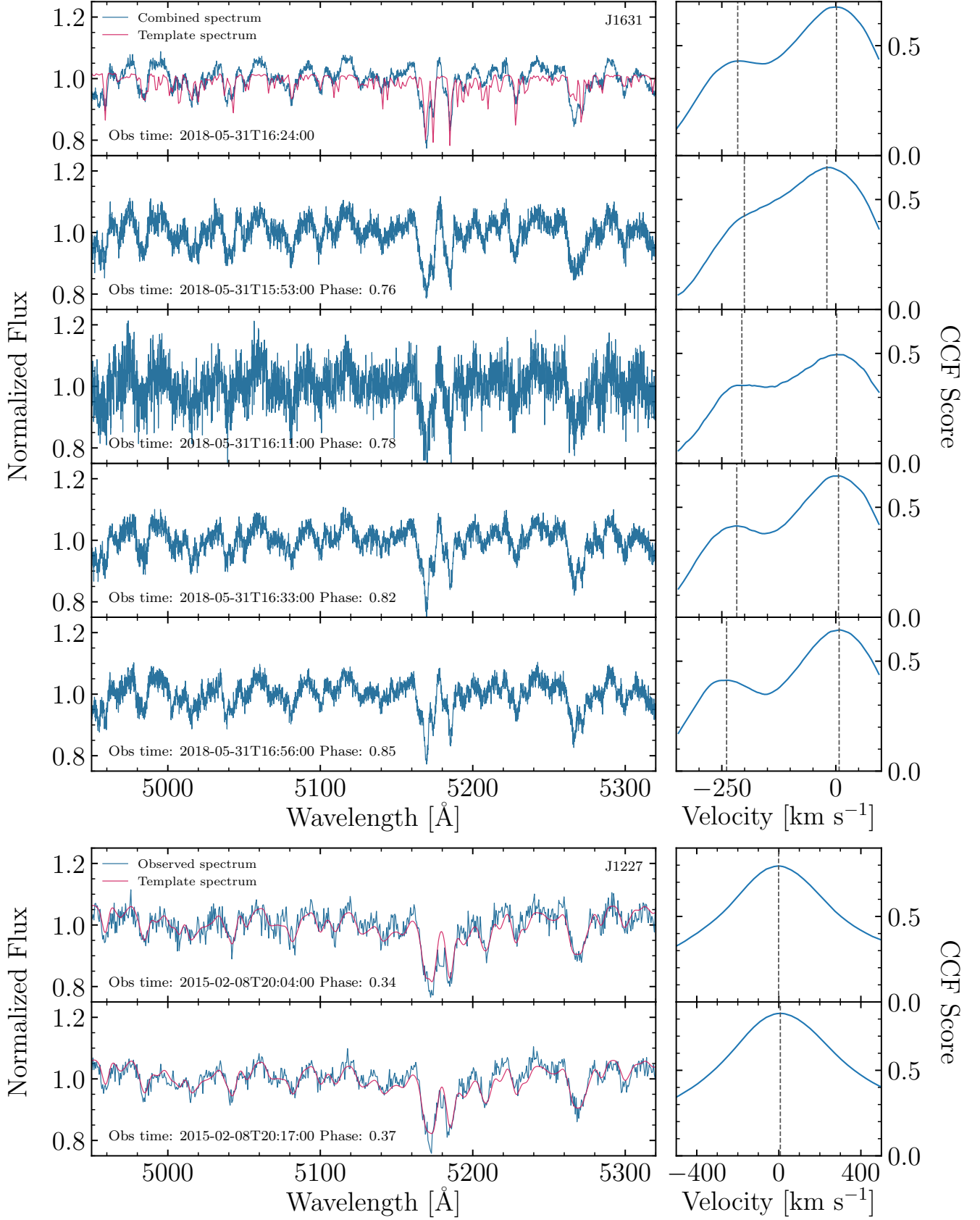


**Figure 4.** LAMOST spectra (left panels) and CCF (right panels) for J1631 (upper panels) and J1227 (lower panels). The uppermost panel in J1631 shows the combined spectrum (blue) and a template spectrum (red) used to measure the CCF profile. The dashed lines mark the peaks in the CCF panels. It is evident from the CCF that J1631 is likely to be a double-lined spectroscopic binary, while J1227 is a single-lined spectroscopic binary. The UTC time for each observation and the corresponding orbital phase is indicated in the figure legend.

perature component measured in four consecutive spectra are  $-202 \text{ km s}^{-1}$ ,  $-212 \text{ km s}^{-1}$ ,  $-213 \text{ km s}^{-1}$ , and  $-216 \text{ km s}^{-1}$ . Another lower temperature component has RVs of  $-2 \text{ km s}^{-1}$ ,  $6 \text{ km s}^{-1}$ ,  $6 \text{ km s}^{-1}$ , and  $8 \text{ km s}^{-1}$ .

For J1227, only the LAMOST LRS survey observed this object twice with an exposure time of 15 minutes each. The template matches the observed spectra well, and the RVs of the two spectra are  $7 \text{ km s}^{-1}$  and  $-1 \text{ km s}^{-1}$ , respectively.

### 3. ANALYZES

The ten targets we selected in Section 2 can be classified into three categories according to their respective observations: two targets (J1227 and J1631, labelled with L in Table 1) have LAMOST spectra; seven targets (J0056, J0216, J0952, J1227, J1631, J2023, and J2305, labelled with P) which have folded light curve periods from *TESS* shorter than the theoretical minimum orbital period; and the remaining three targets (J0623, J0709, and J0805, labelled with C for the first two targets) have no apparent inconsistencies in the parameters. We discuss the three types of targets in the following.

#### 3.1. Spectroscopy

High-quality spectra can be used to estimate whether there are multiple luminous components. To validate the SB1 nature and exclude false positives (potential SB2) of our sample, we check the CCF profiles of each available LAMOST spectrum, by correlating with a best-fitted template. If two or multiple components with similar flux contributions are presented in a high-resolution spectrum, the CCF will feature double or even multiple peaks. Otherwise, if the system has only one dominant component, the CCF will show a single peak, indicating a good correlation between the template and the observation.

We show the LAMOST spectra of the two targets and the corresponding template spectrum used to measure the CCF profile in Figure 4. For J1631, we found that the template cannot match the observed spectra well and the CCFs show clear double peaks. We decomposed the combined spectrum of J1631. The good spectral decomposition (see Figure 5) demonstrates our statement that J1631 is a SB2. As the object has only been observed for less than one hour, we are unable to determine the mass ratio of the binary.

J1227 has two LAMOST LRS spectra, and the template matches well with the observed spectra. Given the current observations, the single-peak feature of both CCFs suggests that J1227 is likely to be a SB1. However, the measured RVs for the two spectra are close to zero, the reason for which will be discussed more in Section 3.2. We stress that more spectroscopic observations with higher spectral resolution and phase coverage are needed to validate the nature of J1227.

#### 3.2. Photometric period and orbital phase

Seven targets in Table 1 have photometric periods shorter than their theoretical minimum period. This indicates a non-physical picture that the radii of the visible stars in these binary systems exceed their Roche radii. One possible reason is that these systems actually consist of two main sequence stars, which are treated as a single star in the pipeline of *Gaia* to measure the stellar parameters. The result is an overestimated stellar radius and hence an overestimated theoretical minimum orbital period. In addition, the photometric period obtained from *TESS* is not necessarily the system's orbital period. It is possible that the photometric variation could have originated from intrinsic variability such as stellar rotation. Due to the lack of additional observations, we cannot rule out these possibilities.

Two targets have spectral observations from LAMOST. Given their orbital ephemeris, we calculated and showed the orbital phase of each LAMOST spectra in Figure 4. The zero points are set to the same as the primary minima of the light curve. Therefore, phase 0.5 corresponds with the scenario that the radial velocities of the two components are both zero.

The LAMOST spectra of J1631 were taken in May 2018, with a two-year gap to *TESS* observations. In order to calculate the orbital phases at which the spectra were taken, we use *TESS* Sector 24 and Sector 25 (from April to June in 2020) in conjunction to achieve a longer observation time span (than just one sector) and therefore to obtain an orbital period with better accuracy. According to our calculation, the four spectra were taken at times corresponding to phases 0.76 - 0.85, which is the case when the radial velocity difference between the two stars is near the maximum. The result is consistent with the double peak shown in the CCF profile.

The radial velocity of J1227 cannot be aligned with its orbital ephemeris. Given the radial velocity variation  $\Delta V_r \simeq 727 \text{ km s}^{-1}$  measured by *Gaia*, it is expected that J1227 should embody a radial velocity variation  $\Delta V_r \simeq 42 \text{ km s}^{-1}$  between the two LAMOST observations, which is correspondingly at phase 0.34 and 0.37. However, CCF measured radial velocity variation  $\Delta V_r \simeq 8 \text{ km s}^{-1}$  disagrees with the expected variation. Considering that only one *TESS* Sector (Sector 22 in 2020) has monitored J1227, which leaves a large time gap of five years with respect to LAMOST observations (in February 2015), the calculated phase at which the LAMOST spectra were taken could therefore suffer from much larger uncertainty due to possible inaccurate period. Photometric observations with a longer time span will help to reduce the uncertainty of period folding and better determine the phases of spectra. Moreover, J1227 could consist of two stars with similar temperatures and luminosities. Since J1227 has only low-resolution spectra taken by LAMOST, the superposition of the two components' spectra with oppo-

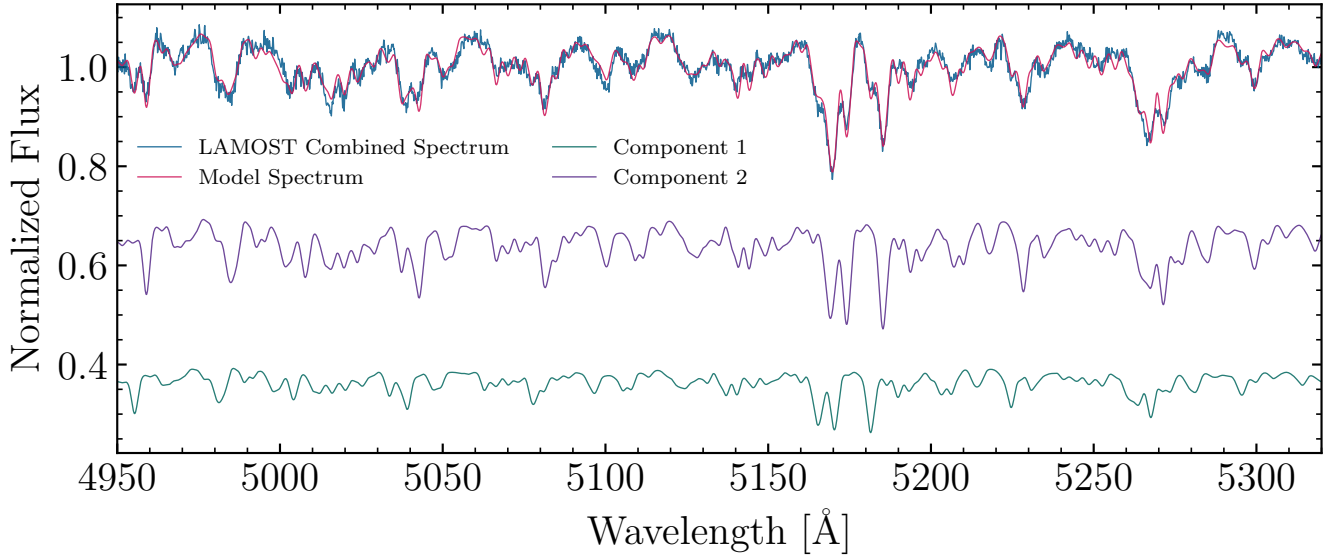


**Figure 5.** Decomposition of the combined spectrum of J1631.

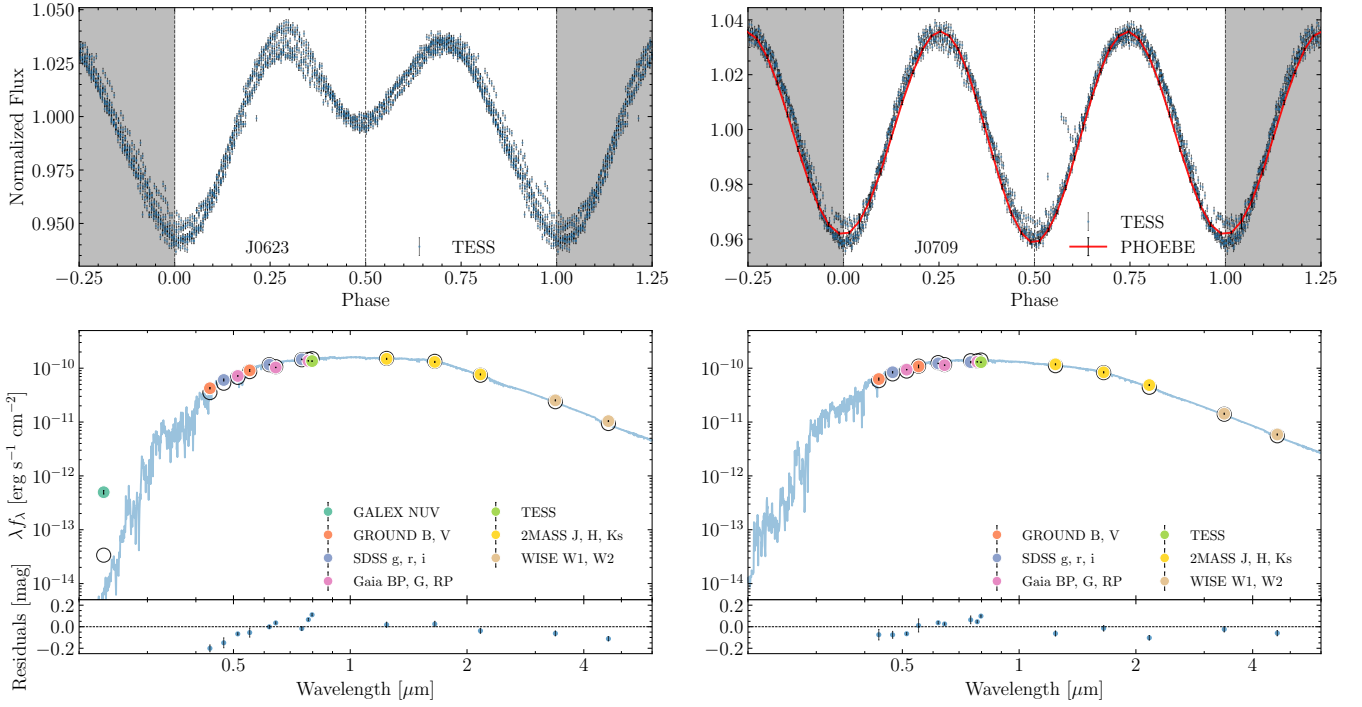


**Figure 6.** The light curves and SED fittings of the two targets with candidate compact objects (J0623 and J0709). Note that the light curves beyond phase 0 - 1 are repeated to better show their ellipsoidal shape, and aligned to ensure the primary minima are in phase 0. The observed *TESS* light curves and the modeled light curves by *PHOEBE* are shown in blue dots and red lines, respectively. The observed values from the same survey are marked by the same color in the SED fitting panels, and the modeled values are marked with black circles.



site RVs will lead to RV smearing on the observed spectra, resulting in CCF measurements yielding two near-zero RVs.

### 3.3. Promising targets

There are two bright stars next to J0805. Due to the interference of these bright stars, we cannot obtain reliable photometric magnitudes of this object, and thus cannot fit the SED. Because of the concern that the photometric magnitudes and the light curves may be contaminated by the surrounding bright stars, we excluded this object from the candidates.

The two remaining targets (J0623 and J0709) in Table 1 satisfy all the criteria listed in Section 2. They have large radial velocity variations, ellipsoidal-like light curves, and their temperatures and radii given by SED fitting are in agreement with the *Gaia* measurements within a  $1.7\sigma$  confidence interval (Figure 6). The lack of X-ray observations queried from HEASARC<sup>6</sup> indicates that J0709 is quiescent. J0623 has X-ray detections by XMM-Newton (Saxton et al. 2008) with a flux range of  $2.714 \times 10^{-12} \sim 3.817 \times 10^{-12} \text{ erg s}^{-1} \text{ cm}^{-2}$ .

We use PHOEBE to fit the light curves of possible pure ellipsoidal targets. As shown in Figure 6, J0709 can be well-fitted by the pure ellipsoidal light curve. However, the light curve of J0623 shows a noticeable difference in depth between its two minima. The two peaks of the light curve are also slightly different, which the pure ellipsoidal model can hardly explain. The observations in multiple TESS sectors show a highly asymmetry and variable light curve (Figure 7). This may indicate the existence of stellar activity on the surface of J0623, and the light curve shape of J0623 could be due to a combination of ellipsoidal variability and stellar activity. The light curve of J0623 is similar to a recently reported white dwarf-main-sequence binary system (Zheng et al. 2022). These two targets contain potential compact objects, and deserve further constraints on their stellar and orbital parameters through follow-up observations.

### 3.4. Radial velocity

Our selection criteria require  $f(M_2) > 1M_\odot$ , which prioritized those targets with large radial velocity variations ( $\Delta V_r > 200 \text{ km s}^{-1}$ ). Blomme et al. (2022) show that the radial velocity measurements of *Gaia* have an average error of  $|\sigma_{V_r}| < 3 \text{ km s}^{-1}$  for targets with  $T_{\text{eff}} < 6000 \text{ K}$ . Katz et al. (2022) present additional bounds for determining whether a target is truly velocity variable. Our criteria fully satisfy these requirements, and it is reasonable to assume that the velocity variation of our samples is credible. However, LAMOST spectra suggest us excluding J1631, which clearly shows double peaks in its CCF profile. In order to exclude

false-positive samples like SB2, and to constrain more precisely on orbital parameters in conjunction with light curves, either the original *Gaia* spectrum or multiple follow-up spectroscopic observations are required.

### 3.5. UV excess

Four of the ten objects (J0056, J0216, J0623, and J1631) have GALEX (Martin et al. 2005) ultraviolet (UV) observations, all of which show near-UV (NUV) excess, that is, the observed NUV flux is higher than the theoretical SED model. For instance, J0623 has an NUV flux of about one magnitude of order larger than the model (e.g., see the left bottom panel of Figure 6). We offer the following two possible indications. (1) Chromospheric activities (Linsky 2017) of the visible star might contribute to a substantial amount of UV excess emission, which the model SED does not contain (model SED contains only the photospheric emissions). The presence of the chromospheric UV emission is supported by the fact that the visible star of J0623 is a spotted rotational star (Figure 7), evidence of wild stellar activities. (2) An accretion process due to the mass transfer from the donor to the compact object might emit UV radiation. This scenario often happens in close binary systems. We stress that however, the conjecture of such an accretion might need to be further examined, using follow-up spectroscopy (i.e., to check whether there is evidence of H $\alpha$  emission line of He emission line by an accretion disk).

### 3.6. Color-magnitude diagram

We show the color-magnitude diagram of the ten targets in Table 1 and 0.28 million randomly selected targets from *Gaia* as background in Figure 8. The color index and extinction-corrected G-band magnitude are provided by *Gaia*. The top-most target J0805 is situated in the giant branch, which may be due to the contamination from the nearby bright stars.

There are seven targets located in the main sequence. We retrieve the color index and magnitude of members of Hyades and Praesepe clusters to distinguish the systems in single star main sequence and others in binary star main sequence (Gaia Collaboration et al. 2018). Four targets (J0216, J1631, J2023, and J2305) are closer with the binary star main sequence. Noteworthy, J1631, a spectroscopically confirmed SB2, is located nearby the binary star main sequence. These possible binary star systems may support one of our explanations about the orbital period conflict: some binary star systems were treated as single star systems in *Gaia*'s pipeline, thus leading to larger radius measurements.

The two targets contain compact object candidates are located on the fringe of the main sequence. Considering they have magnitude exceeds of about 1 - 2 dex above the main sequence, their deviations from the main sequence can hardly be explained by binary star systems. Moreover, the two

<sup>6</sup> <https://heasarc.gsfc.nasa.gov/xamin/xamin.jsp>

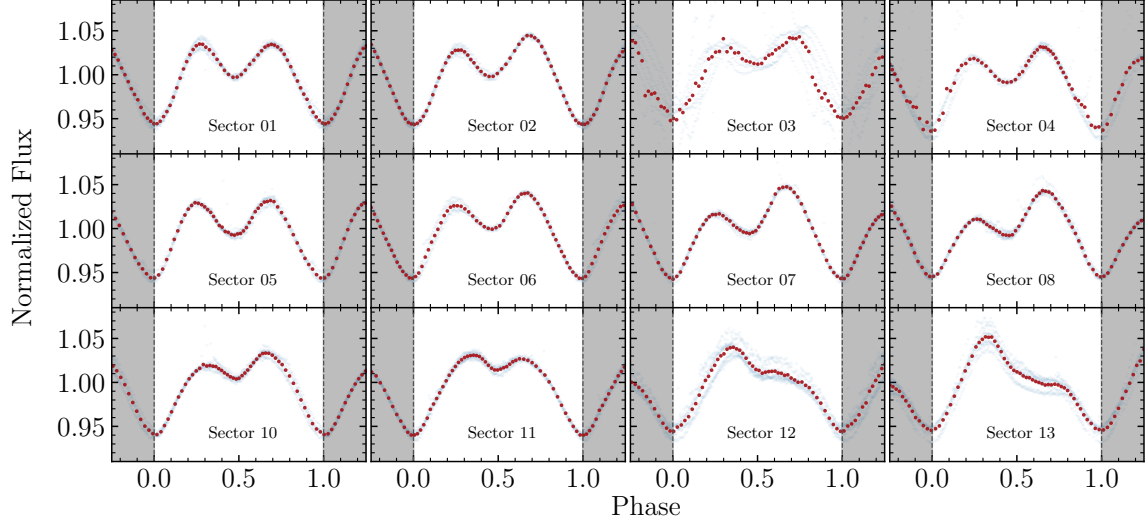


**Figure 7.** The *TESS* light curves of J0623 in multiple sectors. The shallow blue dots show the original normalized flux, and the red dots represent the mean flux of each bin.

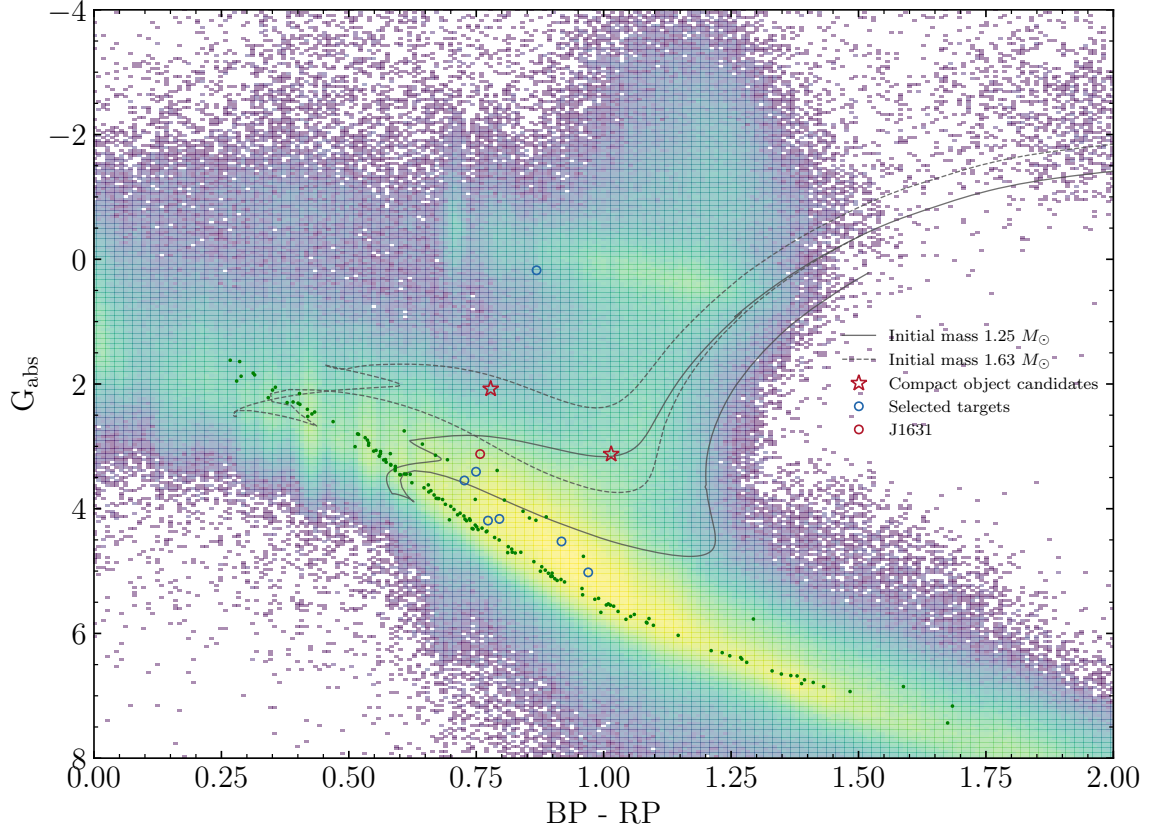


**Figure 8.** The color-magnitude diagram of the ten targets in Table 1. The extinction of G-band magnitude and the BP-RP color reddening have been corrected. The solid and dashed lines show the single star evolution tracks with respective initial masses of 1.25 and 1.63 Solar mass, as suggested by *Gaia*'s measurement. For reference, we plot members of Hyades and Praesepe clusters, using green dots. These members form a clear single-star sequence and a relatively sparse binary-star sequence which lies  $\sim 0.75$  magnitude above.

targets are closer to the subgiant phase in MIST evolution tracks, where the initial masses are set to the same as the *Gaia* measurements. The two targets are more likely to be subgiants which have recently evolved and detached from the main sequence.

#### 4. CONCLUSIONS AND DISCUSSION

In this paper, we try to search for potential compact binary systems from the newly released *Gaia* DR3 database. Based on the radial velocity variations  $\Delta V_r$ , the masses  $M_1$  and radii  $R_1$  of the visible stars provided by *Gaia*, we have selected a sample of 65 sources with mass functions  $f(M_2) > 1M_\odot$ . Ten of these sources have ellipsoidal-like light curves in *TESS*. The properties of these samples are summarized in Table 1.

Utilizing LAMOST spectroscopy available for two of our targets, we exclude one false positive J1631 as a SB2. The other target J1227 is likely to be a SB1 but shows no significant RV variation between two consecutive exposures, therefore the nature of which remains uncertain. J1227 could potentially be a false positive. Although we selected the sources according to criteria very similar to Katz et al. (2022), we still could not completely exclude the potential false-positive targets in the selected samples. Therefore, for targets with large radial velocity variations in *Gaia*, we stress that it is necessary to perform a double check by utilizing spectroscopy from other surveys like LAMOST, or from follow-up observations, to draw a more convincing conclusion.

There are seven targets in Table 1, for which the theoretical minimum orbital periods is larger than the periods calculated by folding the corresponding *TESS* light curves. This contradiction may be attributed to the fact that these sources are in fact binary star systems, while the mass and radius in *Gaia* are mistakenly processed as a single star. We also cannot fully confirm that the folding period of the *TESS* light curve is the true orbital period of the binary system.

Finally, two targets (J0623 and J0709) satisfy all the criteria described in Section 2, and their parameters are more consistent with single-lined spectroscopic binaries. We consider

them as potential compact binary systems. These two are potential compact object candidates and are worth follow-up observations to constrain their stellar parameters. As an illustration, we only study samples with  $f(M_2) > 1M_\odot$ . More worthy targets may be found after loosening the requirement of the mass function. Compared with similar works which dedicated to unveiling compact objects from *Gaia* classified SB1 targets (e.g., El-Badry & Rix 2022; Jayasinghe et al. 2022), we investigate the *Gaia* DR3 main table which contains  $\sim 1.8$  billion objects, thus enabling us to explore more potential candidates. Moreover, utilizing other spectroscopic observations such as LAMOST can prevent our samples from contaminated by false positives. Our work can serve as an example of the dynamical method to search for compact objects in quiescent and demonstrates the potential to filter more compact objects from *Gaia*.

We thank Mouyuan Sun, Qian-Yu An, Hao-Yan Chen, Rui Wang, Jia-Yi Chen, Hao-Bin Liu, and Song Wang for helpful discussions. We thank the anonymous referee for constructive suggestions that improved the paper. This work was supported by the National Key R&D Program of China under grant 2021YFA1600401, the National Natural Science Foundation of China under grants 11925301, 11933004, 11988101, 12033006, 12103041, and 12221003, and the China Postdoctoral Science Foundation under grant 2021M702742. Guoshoujing Telescope (the Large Sky Area Multi-Object Fiber Spectroscopic Telescope, LAMOST) is a National Major Scientific Project built by the Chinese Academy of Sciences. Funding for the project has been provided by the National Development and Reform Commission. LAMOST is operated and managed by the National Astronomical Observatories, Chinese Academy of Sciences.

*Software:* astroARIADNE (Vines & Jenkins 2022), Astropy (Astropy Collaboration et al. 2013, 2018), Lightkurve (Lightkurve Collaboration et al. 2018), Matplotlib (Hunter 2007), MIST (Dotter 2016), NumPy (Harris et al. 2020), pandas (Wes McKinney 2010), PHOEBE (Conroy et al. 2020), The Payne (Ting et al. 2019)

**Table 1.** Characteristics of selected targets from *Gaia* DR3

ID	<i>Gaia</i> Source ID	R.A.	Dec	$M_1$	$R_1$	$\Delta V_r$	$T_{\text{eff}}$	$P_{\text{orb}}^{\text{min}}$	$P_{\text{orb}}^{\text{le}}$	$f(M_2)_{\text{Gaia}}$	$f(M_2)_{\text{le}}$	$T_{\text{eff,SED}}$	$R_{1,\text{SED}}$	$BP - RP$	$G_{\text{abs}}$	Label
				( $M_{\odot}$ )	( $R_{\odot}$ )	( $\text{km s}^{-1}$ )	(K)	(days)	(days)	( $M_{\odot}$ )	( $M_{\odot}$ )	(K)	( $R_{\odot}$ )	(11)	(12)	(13)
J0056	4987200236093193216	00:56:18.0	-41:21:56.45	0.963	$1.30^{+0.03}_{-0.08}$	603.115	$5704^{+70}_{-19}$	0.559	0.334	1.59	0.95	$5810^{+203}_{-262}$	$1.26^{+0.11}_{-0.11}$	0.795	4.16	P
J0216	4944640992840656000	02:16:25.3	-43:12:10.58	1.106	$1.58^{+0.02}_{-0.01}$	616.590	$5927^{+35}_{-27}$	0.697	0.416	2.12	1.26	$5919^{+247}_{-256}$	$1.62^{+0.12}_{-0.10}$	0.727	3.55	P
J0623	5284413278650095872	06:23:34.3	-66:17:18.99	1.251	$2.74^{+0.08}_{-0.14}$	452.383	$5061^{+47}_{-26}$	1.497	3.562	1.79	4.27	$4798^{+135}_{-131}$	$3.08^{+0.20}_{-0.20}$	1.015	3.12	C
J0709	5602540372393859968	07:09:01.9	-34:51:56.10	1.627	$3.31^{+0.01}_{-0.01}$	393.256	$5918^{+6}_{-6}$	1.739	3.513	1.37	2.77	$5480^{+248}_{-248}$	$3.74^{+0.39}_{-0.28}$	0.778	2.08	C
J0805	5546086050952797952	08:05:09.5	-33:33:04.76	2.401	$9.20^{+0.28}_{-0.16}$	242.124	$5575^{+9}_{-11}$	6.638	7.019	1.22	1.29	...	...	0.868	0.18	...
J0952	5687390848640176000	09:52:58.8	-13:48:29.50	0.991	$1.23^{+0.01}_{-0.01}$	590.239	$5798^{+3}_{-4}$	0.504	0.450	1.34	1.20	$5449^{+224}_{-382}$	$1.38^{+0.17}_{-0.10}$	0.773	4.19	P
J1227	1542461401838152960	12:27:29.4	+47:44:19.35	0.906	$1.12^{+0.01}_{-0.03}$	726.781	$5128^{+11}_{-12}$	0.461	0.273	2.29	1.36	$4876^{+175}_{-383}$	$1.22^{+0.11}_{-0.15}$	0.970	5.02	LP
J1631	1410477980245374848	16:31:55.3	+47:35:10.51	1.193	$1.88^{+0.02}_{-0.02}$	472.610	$5936^{+7}_{-7}$	0.872	0.476	1.19	0.65	$5836^{+181}_{-132}$	$1.98^{+0.11}_{-0.10}$	0.758	3.12	LP
J2023	2243723836359839872	20:23:48.9	+63:33:43.03	0.908	$1.27^{+0.02}_{-0.01}$	579.668	$5340^{+51}_{-78}$	0.555	0.301	1.40	0.76	$5288^{+192}_{-210}$	$1.29^{+0.09}_{-0.09}$	0.917	4.53	P
J2305	1931538743969686912	23:05:51.3	+42:32:43.32	1.116	$1.76^{+0.04}_{-0.04}$	611.487	$5825^{+42}_{-39}$	0.812	0.428	2.40	1.27	$5789^{+265}_{-172}$	$1.79^{+0.10}_{-0.19}$	0.748	3.41	P

NOTE—(1 - 4) The mass ( $M_1$ ), radius ( $R_1$ ), radial velocity variation ( $\Delta V_r$ ), and temperature ( $T_{\text{eff}}$ ) measured by *Gaia*. (5) The theoretical minimum orbital period ( $P_{\text{orb}}^{\text{min}}$ ) calculated from the *Gaia* parameters. (6) The photometric period ( $P_{\text{orb}}^{\text{le}}$ ) folded from the *TES* light curve. (7) The mass function of the invisible components ( $f(M_2)_{\text{Gaia}}$ ) calculated from  $P_{\text{orb}}^{\text{min}}$ . (8) The mass function of the invisible components ( $f(M_2)_{\text{le}}$ ) calculated from  $P_{\text{orb}}^{\text{le}}$ . (9 - 10) The temperature ( $T_{\text{eff,SED}}$ ) and radius ( $R_{1,\text{SED}}$ ) measured by SED fitting. (11 - 12) The color index ( $B_P - R_P$ ) and G band magnitude ( $G_{\text{abs}}$ ) measured by *Gaia*. (13) The label used to separate targets into different categories: C for a probably compact object candidate, L for a target with LAMOST spectroscopic observations, and P for a target with a photometric period shorter than the theoretical minimum orbital period.

## APPENDIX

## A. FULL SELECTED SAMPLES

**Table 2.** Characteristics of 65 selected targets from *Gaia* DR3

<i>Gaia</i> Source ID	R.A.	Dec	$M_1$	$R_1$	$\Delta V_r$	$T_{\text{eff}}$	$P_{\text{orb}}^{\text{min}}$	$P_{\text{orb}}^{\text{lc}}$	$f(M_2)_{\text{Gaia}}$	$f(M_2)_{\text{lc}}$
			(1)	(2)	(3)	(4)	(5)	(6)	(7)	(8)
			( $M_{\odot}$ )	( $R_{\odot}$ )	( $\text{km s}^{-1}$ )	(K)	(days)	(days)	( $M_{\odot}$ )	( $M_{\odot}$ )
431341435235181056	00:13:09.1	+63:09:20.27	4.687	33.892	169.310	5879	33.616	40.000	2.11	2.51
524536457422822016	00:51:23.5	+65:13:05.60	5.333	4.479	487.597	5762	1.514	2.326	2.27	3.49
423647194605271808	00:52:08.6	+55:35:43.56	1.142	8.148	223.900	4417	8.028	5.955	1.17	0.87
4987200236093193216	00:56:18.0	-41:21:56.45	0.963	1.302	603.115	5704	0.559	0.334	1.59	0.95
297802831758073984	01:58:29.6	+26:03:33.13	1.140	1.922	496.225	5675	0.921	0.455	1.46	0.72
346272671566816512	02:03:09.3	+42:36:51.00	2.501	7.509	304.104	5209	4.799	20.756	1.75	7.56
508371746710670976	02:04:55.0	+60:55:45.07	6.112	4.694	654.221	5982	1.517	28.465	5.50	103.22
4944640992840656000	02:16:25.3	-43:12:10.58	1.106	1.581	616.590	5927	0.697	0.416	2.12	1.26
516035548914422400	02:30:10.9	+64:58:32.51	1.085	1.689	609.841	5723	0.777	0.391	2.28	1.15
5079746164163047296	03:03:13.4	-20:36:50.98	1.056	1.228	610.946	5917	0.489	0.335	1.44	0.99
5099527782799972736	03:16:12.0	-22:05:30.87	1.097	1.868	565.268	5589	0.899	0.772	2.10	1.81
4853820950132560896	03:17:55.4	-39:16:48.76	1.095	1.501	530.947	5955	0.648	1.650	1.26	3.20
5086274102138599808	03:33:07.0	-24:17:00.10	0.965	1.391	542.507	5636	0.616	...	1.27	...
2915702118705099520	05:53:02.8	-23:22:28.60	1.057	1.260	582.941	5891	0.507	0.337	1.30	0.86
3344011302729909760	06:09:17.0	+12:32:48.48	3.396	15.443	205.060	5169	12.147	30.046	1.36	3.36
5284413278650095872	06:23:34.3	-66:17:18.99	1.251	2.741	452.383	5061	1.497	3.562	1.79	4.27
2922949687038297088	06:33:30.0	-26:22:16.05	0.993	1.333	1083.699	5775	0.570	0.679	9.39	11.19
2928949511533366784	07:03:14.2	-21:21:47.26	0.929	1.305	608.021	5530	0.571	0.411	1.66	1.20
5602540372393859968	07:09:01.9	-34:51:56.10	1.627	3.307	393.256	5918	1.739	3.513	1.37	2.77
5275788125325011584	07:47:57.6	-64:44:23.35	1.080	2.979	710.641	4925	1.825	2.227	8.48	10.35
5546086050952797952	08:05:09.5	-33:33:04.76	2.401	9.195	242.124	5575	6.638	7.019	1.22	1.29
707471754641398144	08:22:35.5	+28:55:18.70	1.070	4.244	317.901	4804	3.118	...	1.30	...
1123617153201142656	08:25:58.6	+74:51:01.39	1.103	1.311	572.739	5993	0.527	0.417	1.28	1.02
5709247009497151872	08:38:14.9	-16:58:31.49	1.050	1.727	709.356	5603	0.817	0.662	3.78	3.06
5709342980542992768	08:45:05.3	-16:25:02.77	0.900	1.040	729.708	5577	0.413	0.665	2.08	3.34
5325906785898343168	09:10:21.0	-49:23:24.86	1.597	3.247	415.958	5572	1.708	0.767	1.59	0.71
714884906850837120	09:16:12.2	+36:15:33.34	0.842	1.211	585.521	4719	0.536	0.367	1.39	0.95
5435132408441359360	09:47:54.0	-35:17:26.66	0.931	1.356	664.705	5516	0.604	0.327	2.30	1.24
5687390848640176000	09:52:58.8	-13:48:29.50	0.991	1.228	590.239	5798	0.504	0.450	1.34	1.20
5200508962219751424	11:26:40.6	-77:10:14.43	6.617	178.770	501.350	3315	342.744	30.657	559.35	50.03
1542461401838152960	12:27:29.4	+47:44:19.35	0.906	1.123	726.781	5128	0.461	0.273	2.29	1.36
6127569097490978944	12:32:38.4	-48:58:46.68	0.834	0.761	1064.489	5028	0.268	0.238	4.19	3.72
3745090711928464512	13:28:22.2	+15:50:07.71	1.423	4.948	381.228	4923	3.403	4.767	2.44	3.42
5864984550877297280	13:33:44.0	-63:40:18.36	4.101	6.066	466.367	5480	2.721	30.046	3.57	39.47
5846761386917033600	14:20:27.4	-68:26:19.33	2.496	7.522	334.953	5412	4.816	24.487	2.34	11.92
5785826933521556096	14:28:49.0	-78:04:46.02	1.271	2.141	497.625	5982	1.025	0.850	1.64	1.36
4429810650412646528	15:43:19.6	+06:39:15.87	1.050	1.776	621.893	5505	0.852	...	2.65	...
5819146877495757568	15:50:47.4	-70:21:46.30	2.803	8.855	324.515	4856	5.806	17.370	2.57	7.69
5820369946745384832	15:51:00.8	-68:49:32.34	2.354	9.470	280.023	4907	7.006	9.687	1.99	2.75
5931568402480842496	16:17:57.2	-55:56:22.89	0.882	0.852	698.242	5328	0.309	0.249	1.36	1.10
5944159666018686848	16:27:46.6	-43:56:32.63	2.494	9.253	285.196	5266	6.574	37.976	1.98	11.41
1410477980245374848	16:31:55.3	+47:35:10.52	1.193	1.882	472.610	5936	0.872	0.476	1.19	0.65
4126243594591367168	16:53:45.5	-21:51:49.28	2.187	5.615	505.349	5618	3.319	...	5.55	...

**Table 2** continued



Table 2 (continued)

<i>Gaia</i> Source ID	R.A.	Dec	$M_1$	$R_1$	$\Delta V_r$	$T_{\text{eff}}$	$P_{\text{orb}}^{\text{min}}$	$P_{\text{orb}}^{\text{lc}}$	$f(M_2)_{\text{Gaia}}$	$f(M_2)_{\text{lc}}$
			(1)	(2)	(3)	(4)	(5)	(6)	(7)	(8)
			( $M_{\odot}$ )	( $R_{\odot}$ )	(km s $^{-1}$ )	(K)	(days)	(days)	( $M_{\odot}$ )	( $M_{\odot}$ )
4549835637507855104	17:30:41.8	+16:12:19.14	1.138	1.754	623.865	5750	0.803	0.516	2.52	1.62
4596507058545940096	17:54:04.6	+28:57:49.06	2.446	7.710	299.051	5316	5.049	11.272	1.75	3.90
2153650709938721280	18:51:22.8	+57:28:19.36	0.940	1.435	528.804	5456	0.654	0.398	1.25	0.76
4514619143398364800	19:06:08.2	+18:05:23.58	1.685	3.364	475.779	5834	1.753	...	2.45	...
4306343947116038656	19:10:29.8	+07:09:18.36	1.112	1.738	506.247	5800	0.802	...	1.35	...
4294229905988953856	19:32:11.7	+05:22:58.40	2.299	7.053	322.304	5204	4.557	...	1.98	...
2025421609519820160	19:37:07.6	+28:10:53.60	3.301	14.351	202.179	5026	11.038	...	1.18	...
2048262142478593280	19:38:46.2	+35:53:15.35	0.971	1.262	556.966	5727	0.531	0.304	1.19	0.68
2087298894057921536	19:51:59.2	+50:05:29.32	0.996	1.500	531.876	5647	0.679	0.387	1.32	0.75
2029905482299047040	20:11:06.6	+30:38:54.25	1.126	1.814	617.427	5767	0.849	...	2.59	...
2062243493661150720	20:18:31.9	+39:57:28.40	5.710	5.961	423.467	5866	2.246	4.677	2.21	4.60
2060993353245576448	20:20:52.2	+37:48:18.97	5.035	4.544	706.794	5761	1.592	31.347	7.28	143.34
2054348862739979648	20:23:38.7	+32:17:29.13	1.187	1.887	519.595	5912	0.878	29.823	1.59	54.18
2243723836359839872	20:23:48.9	+63:33:43.03	0.908	1.271	579.668	5340	0.555	0.301	1.40	0.76
6425649173675248768	20:25:22.6	-66:33:49.97	1.011	1.519	514.342	5743	0.687	0.616	1.21	1.09
4218379306035449216	20:35:27.0	-04:49:38.79	1.018	1.457	568.020	5744	0.643	...	1.53	...
2066328011855804544	20:39:56.6	+41:22:25.27	6.413	125.273	116.742	4073	204.228	11.785	4.21	0.24
1859677511539011456	20:51:40.8	+31:39:32.67	1.408	2.137	570.741	5967	0.971	1.129	2.34	2.72
1844666360320230144	20:59:35.1	+26:14:23.74	1.303	2.266	439.616	5949	1.102	0.493	1.21	0.54
1977530417708089728	21:37:23.6	+47:04:53.23	1.048	1.627	539.573	5715	0.748	0.391	1.52	0.80
1987682247232185088	22:27:55.3	+48:54:36.02	1.638	3.433	588.116	5485	1.833	8.539	4.83	22.50
1931538743969686912	23:05:51.3	+42:32:43.33	1.116	1.755	611.487	5825	0.812	0.428	2.40	1.27

NOTE—(1 - 4) The mass ( $M_1$ ), radius ( $R_1$ ), radial velocity variation ( $\Delta V_r$ ), and temperature ( $T_{\text{eff}}$ ) measured by *Gaia*. (5) The theoretical minimum orbital period ( $P_{\text{orb}}^{\text{min}}$ ) calculated from the *Gaia* parameters. (6) The photometric period ( $P_{\text{orb}}^{\text{lc}}$ ) folded from the *TESS* light curve. (7) The mass function of the invisible components ( $f(M_2)_{\text{Gaia}}$ ) calculated from  $P_{\text{orb}}^{\text{min}}$ . (8) The mass function of the invisible components ( $f(M_2)_{\text{lc}}$ ) calculated from  $P_{\text{orb}}^{\text{lc}}$ .

## REFERENCES

- Abbott, B. P., Abbott, R., Abbott, T. D., et al. 2016, *Physical Review X*, 6, 041015, doi: [10.1103/PhysRevX.6.041015](https://doi.org/10.1103/PhysRevX.6.041015)
- Astropy Collaboration, Robitaille, T. P., Tollerud, E. J., et al. 2013, *A&A*, 558, A33, doi: [10.1051/0004-6361/201322068](https://doi.org/10.1051/0004-6361/201322068)
- Astropy Collaboration, Price-Whelan, A. M., Sipőcz, B. M., et al. 2018, *AJ*, 156, 123, doi: [10.3847/1538-3881/aabc4f](https://doi.org/10.3847/1538-3881/aabc4f)
- Blomme, R., Fremat, Y., Sartoretti, P., et al. 2022, arXiv e-prints, arXiv:2206.05486. <https://arxiv.org/abs/2206.05486>
- Bohlin, R. C., Mészáros, S., Fleming, S. W., et al. 2017, *AJ*, 153, 234, doi: [10.3847/1538-3881/aa6ba9](https://doi.org/10.3847/1538-3881/aa6ba9)
- Casares, J., Negueruela, I., Ribó, M., et al. 2014, *Nature*, 505, 378, doi: [10.1038/nature12916](https://doi.org/10.1038/nature12916)
- Cojocaru, R., Rebassa-Mansergas, A., Torres, S., & García-Berro, E. 2017, *MNRAS*, 470, 1442, doi: [10.1093/mnras/stx1326](https://doi.org/10.1093/mnras/stx1326)
- Conroy, K. E., Kochoska, A., Hey, D., et al. 2020, *ApJS*, 250, 34, doi: [10.3847/1538-4365/abb4e2](https://doi.org/10.3847/1538-4365/abb4e2)
- Cui, X.-Q., Zhao, Y.-H., Chu, Y.-Q., et al. 2012, *Research in Astronomy and Astrophysics*, 12, 1197, doi: [10.1088/1674-4527/12/9/003](https://doi.org/10.1088/1674-4527/12/9/003)
- De Angeli, F., Weiler, M., Montegriffo, P., et al. 2022, arXiv e-prints, arXiv:2206.06143. <https://arxiv.org/abs/2206.06143>
- Dotter, A. 2016, *ApJS*, 222, 8, doi: [10.3847/0067-0049/222/1/8](https://doi.org/10.3847/0067-0049/222/1/8)
- El-Badry, K., & Rix, H.-W. 2022, *MNRAS*, doi: [10.1093/mnras/stac1797](https://doi.org/10.1093/mnras/stac1797)
- El-Badry, K., Ting, Y.-S., Rix, H.-W., et al. 2018, *MNRAS*, 476, 528, doi: [10.1093/mnras/sty240](https://doi.org/10.1093/mnras/sty240)
- El-Badry, K., Rix, H.-W., Quataert, E., et al. 2022, arXiv e-prints, arXiv:2209.06833. <https://arxiv.org/abs/2209.06833>
- Gaia* Collaboration, Babusiaux, C., van Leeuwen, F., et al. 2018, *A&A*, 616, A10, doi: [10.1051/0004-6361/201832843](https://doi.org/10.1051/0004-6361/201832843)
- Gomel, R., Faigler, S., & Mazeh, T. 2021, *MNRAS*, 501, 2822, doi: [10.1093/mnras/staa3305](https://doi.org/10.1093/mnras/staa3305)
- Gomel, R., Mazeh, T., Faigler, S., et al. 2022, arXiv e-prints, arXiv:2206.06032. <https://arxiv.org/abs/2206.06032>

- Gu, W.-M., Mu, H.-J., Fu, J.-B., et al. 2019, *ApJL*, 872, L20, doi: [10.3847/2041-8213/ab04f0](https://doi.org/10.3847/2041-8213/ab04f0)
- Hambly, N., Andrae, R., De Angeli, F., et al. 2022, *Gaia* DR3 documentation Chapter 20: Datamodel description
- Harris, C. R., Millman, K. J., van der Walt, S. J., et al. 2020, *Nature*, 585, 357, doi: [10.1038/s41586-020-2649-2](https://doi.org/10.1038/s41586-020-2649-2)
- Hernandez, M. S., Schreiber, M. R., Parsons, S. G., et al. 2021, *MNRAS*, 501, 1677, doi: [10.1093/mnras/staa3815](https://doi.org/10.1093/mnras/staa3815)
- Holl, B., Sozzetti, A., Sahlmann, J., et al. 2022, arXiv e-prints, arXiv:2206.05439. <https://arxiv.org/abs/2206.05439>
- Hunter, J. D. 2007, *Computing in Science & Engineering*, 9, 90, doi: [10.1109/MCSE.2007.55](https://doi.org/10.1109/MCSE.2007.55)
- Janssens, S., Shenar, T., Sana, H., et al. 2022, *A&A*, 658, A129, doi: [10.1051/0004-6361/202141866](https://doi.org/10.1051/0004-6361/202141866)
- Jayasinghe, T., Rowan, D. M., Thompson, T. A., Kochanek, C. S., & Stanek, K. Z. 2022, arXiv e-prints, arXiv:2207.05086. <https://arxiv.org/abs/2207.05086>
- Jayasinghe, T., Stanek, K. Z., Thompson, T. A., et al. 2021, *MNRAS*, 504, 2577, doi: [10.1093/mnras/stab907](https://doi.org/10.1093/mnras/stab907)
- Katz, D., Sartoretti, P., Guerrier, A., et al. 2022, arXiv e-prints, arXiv:2206.05902. <https://arxiv.org/abs/2206.05902>
- Lam, C. Y., Lu, J. R., Udalski, A., et al. 2022, *ApJL*, 933, L23, doi: [10.3847/2041-8213/ac7442](https://doi.org/10.3847/2041-8213/ac7442)
- Li, C.-q., Shi, J.-r., Yan, H.-l., et al. 2021, *ApJS*, 256, 31, doi: [10.3847/1538-4365/ac22a8](https://doi.org/10.3847/1538-4365/ac22a8)
- Lightkurve Collaboration, Cardoso, J. V. d. M., Hedges, C., et al. 2018, *Lightkurve: Kepler and TESS time series analysis in Python*, *Astrophysics Source Code Library*. <http://ascl.net/1812.013>
- Linsky, J. L. 2017, *ARA&A*, 55, 159, doi: [10.1146/annurev-astro-091916-055327](https://doi.org/10.1146/annurev-astro-091916-055327)
- Liu, J., Zhang, H., Howard, A. W., et al. 2019, *Nature*, 575, 618, doi: [10.1038/s41586-019-1766-2](https://doi.org/10.1038/s41586-019-1766-2)
- Martin, D. C., Fanson, J., Schiminovich, D., et al. 2005, *ApJL*, 619, L1, doi: [10.1086/426387](https://doi.org/10.1086/426387)
- Mazeh, T., Faigler, S., Bashi, D., et al. 2022, arXiv e-prints, arXiv:2206.11270. <https://arxiv.org/abs/2206.11270>
- McClintock, J. E., & Remillard, R. A. 2006, in *Compact stellar X-ray sources*, Vol. 39, 157–213
- Merle, T., Van Eck, S., Jorissen, A., et al. 2017, *A&A*, 608, A95, doi: [10.1051/0004-6361/201730442](https://doi.org/10.1051/0004-6361/201730442)
- Montegriffo, P., De Angeli, F., Andrae, R., et al. 2022, arXiv e-prints, arXiv:2206.06205. <https://arxiv.org/abs/2206.06205>
- Morris, S. L. 1985, *ApJ*, 295, 143, doi: [10.1086/163359](https://doi.org/10.1086/163359)
- Morris, S. L., & Naftilan, S. A. 1993, *ApJ*, 419, 344, doi: [10.1086/173488](https://doi.org/10.1086/173488)
- Mu, H.-J., Gu, W.-M., Yi, T., et al. 2022, *Science China Physics, Mechanics, and Astronomy*, 65, 229711, doi: [10.1007/s11433-021-1809-8](https://doi.org/10.1007/s11433-021-1809-8)
- Press, W. H., & Rybicki, G. B. 1989, *ApJ*, 338, 277, doi: [10.1086/167197](https://doi.org/10.1086/167197)
- Rebassa-Mansergas, A., Ren, J. J., Parsons, S. G., et al. 2016, *MNRAS*, 458, 3808, doi: [10.1093/mnras/stw554](https://doi.org/10.1093/mnras/stw554)
- Rebassa-Mansergas, A., Ren, J. J., Irawati, P., et al. 2017, *MNRAS*, 472, 4193, doi: [10.1093/mnras/stx2259](https://doi.org/10.1093/mnras/stx2259)
- Recio-Blanco, A., de Laverny, P., Palicio, P. A., et al. 2022, arXiv e-prints, arXiv:2206.05541. <https://arxiv.org/abs/2206.05541>
- Remillard, R. A., & McClintock, J. E. 2006, *ARA&A*, 44, 49, doi: [10.1146/annurev.astro.44.051905.092532](https://doi.org/10.1146/annurev.astro.44.051905.092532)
- Ren, J. J., Rebassa-Mansergas, A., Parsons, S. G., et al. 2018, *MNRAS*, 477, 4641, doi: [10.1093/mnras/sty805](https://doi.org/10.1093/mnras/sty805)
- Ricker, G. R., Winn, J. N., Vanderspek, R., et al. 2015, *Journal of Astronomical Telescopes, Instruments, and Systems*, 1, 014003, doi: [10.1117/1.JATIS.1.1.014003](https://doi.org/10.1117/1.JATIS.1.1.014003)
- Rivinius, T., Baade, D., Hadrava, P., Heida, M., & Klement, R. 2020, *A&A*, 637, L3, doi: [10.1051/0004-6361/202038020](https://doi.org/10.1051/0004-6361/202038020)
- Rowan, D. M., Stanek, K. Z., Jayasinghe, T., et al. 2021, *MNRAS*, 507, 104, doi: [10.1093/mnras/stab2126](https://doi.org/10.1093/mnras/stab2126)
- Saracino, S., Kamann, S., Guarcello, M. G., et al. 2022, *MNRAS*, 511, 2914, doi: [10.1093/mnras/stab3159](https://doi.org/10.1093/mnras/stab3159)
- Saxton, R. D., Read, A. M., Esquej, P., et al. 2008, *A&A*, 480, 611, doi: [10.1051/0004-6361:20079193](https://doi.org/10.1051/0004-6361:20079193)
- Shenar, T., Sana, H., Mahy, L., et al. 2022, arXiv e-prints, arXiv:2207.07675. <https://arxiv.org/abs/2207.07675>
- Thompson, T. A., Kochanek, C. S., Stanek, K. Z., et al. 2019, *Science*, 366, 637, doi: [10.1126/science.aau4005](https://doi.org/10.1126/science.aau4005)
- Ting, Y.-S., Conroy, C., Rix, H.-W., & Cargile, P. 2019, *ApJ*, 879, 69, doi: [10.3847/1538-4357/ab2331](https://doi.org/10.3847/1538-4357/ab2331)
- Vines, J. I., & Jenkins, J. S. 2022, *MNRAS*, doi: [10.1093/mnras/stac956](https://doi.org/10.1093/mnras/stac956)
- Wes McKinney. 2010, in *Proceedings of the 9th Python in Science Conference*, ed. Stéfan van der Walt & Jarrod Millman, 56 – 61, doi: [10.25080/Majora-92bf1922-00a](https://doi.org/10.25080/Majora-92bf1922-00a)
- Zhang, Z.-X., Zheng, L.-L., Gu, W.-M., et al. 2022, *ApJ*, 933, 193, doi: [10.3847/1538-4357/ac75b6](https://doi.org/10.3847/1538-4357/ac75b6)
- Zhao, G., Zhao, Y.-H., Chu, Y.-Q., Jing, Y.-P., & Deng, L.-C. 2012, *Research in Astronomy and Astrophysics*, 12, 723, doi: [10.1088/1674-4527/12/7/002](https://doi.org/10.1088/1674-4527/12/7/002)
- Zheng, L.-L., Gu, W.-M., Yi, T., et al. 2019, *AJ*, 158, 179, doi: [10.3847/1538-3881/ab449f](https://doi.org/10.3847/1538-3881/ab449f)
- Zheng, L.-L., Gu, W.-M., Sun, M., et al. 2022, *ApJ*, 936, 33, doi: [10.3847/1538-4357/ac853f](https://doi.org/10.3847/1538-4357/ac853f)